Effect of Pressurization on Solid Oxide Cell Oxygen Electrodes:

the Role of PrOx Nanoparticle Infiltration

Authors

Jerren Grimes[a] and Scott A. Barnett[a] *

[a] Department of Materials Science and Engineering, Northwestern University, Evanston, Illinois 60208, USA

* Corresponding author

E-mail: s-barnett@northwestern.edu

Abstract

Pressurization of solid oxide cells improves performance by reducing electrode polarization resistance (R_P) and facilitates system integration with balance of plant components such as pressurized storage tanks. However, there are few reports on pressurization effects for electrodes designed for low-temperature operation and utilizing infiltrated catalysts. Here we report an electrochemical impedance spectroscopy study of high performing oxygen electrode materials, $SrTi_{0.3}Fe_{0.63}Co_{0.07}O_{3-\partial}$ (STFC) and PrO_x infiltrated STFC, for oxygen partial pressures (p_{O_2}) from 0.1 to 8 atm and temperatures from 550 to 650 ˚C. R_P decreases more with pressurization for STFC:PrO_x, fitting well to $R_P \propto p_{O_2}^{-n}$ with an exponent n~0.3, compared to n~0.25 for STFC. The combination of PrO_x infiltration and pressurization yields a substantial R_P decrease, *e.g.,* at 600 ˚C by ~7 times from 0.36 Ω cm^2 at p_{O_2} = 0.2 atm for STFC to 0.055 Ω cm^2 at p_{O_2} = 4 atm for STFC:PrO_x. A transmission-line-based circuit model impedance fit reveals that the significant oxygen surface reaction (R_{surf}) resistance contribution decreases substantially with PrO_x infiltration; and its p_{O_2} dependence become more pronounced, with *n* increasing from ~ 0.25 to ~ 0.5. R_{surf} for STFC:PrO_x decreases so much at elevated p_{O_2} that the electrode/electrolyte interface resistance dominates.

Keywords: solid oxide cell; infiltrated electrode; energy storage

1. Introduction

Pressurization of solid oxide cells (SOC) has been proposed for a number of applications such as combined SOC-turbine cycles,[1, 2] integration of SOC electrolyzers with downstream catalytic processes,[3] and reversible SOCs for energy storage.[4, 5] Pressurized operation can provide system-level advantages; for electrolysis and reversible SOC systems, for example, considerable improvements in process efficiency are expected.[6-10] For the reversible application, the SOCs should also have very low ASR in order to achieve high round-trip efficiency, and ideally operate at relatively low temperature.[7, 9, 10] Pressurized operation has advantages in this regard because of improved cell performance compared to ambient pressure operation, a result of reduced electrode polarization resistance.[11-14] Fundamentally, an increase in O_2 partial pressure increases the extent of adsorption of O_2 gas molecules onto the electrode surface. From the linearized form of the Butler-Volmer equation, this results in an increase in exchange current density, i.e. faster reaction kinetics and thus a lower charge transfer resistance. Pressurization-induced reduction of cell area-specific resistance can help compensate for the increase caused by reduced operating temperature, thereby helping to enable low temperature SOCs (LT-SOCs).[15-17]

The oxygen electrode is generally believed to be the main factor limiting LT-SOC performance because of the high activation energy of the ORR reaction.[15] Pressurization has generally been observed to reduce oxygen electrode polarization resistance R_P, but the amount of the reduction varies widely.[11-13] While the effect of pressurization has been established for the standard SOC oxygen electrode LSM-YSZ,[3, 11, 18] less is known about the plethora of mixed ionic electronic conductor (MIEC) oxygen electrodes that have been developed for LT-SOCs. LSCF, a widely used MIEC electrode, shows only a minor reduction in R_P with increasing p_{O_2} up to 10 atm, following $R_P \propto p_{O_2}^{-n}$ with a relatively low n value of 0.11,[14] explained by a reduction in oxygen vacancy concentration with increasing p_{O_2}. Other MIEC types such as nickelates, which conduct via oxygen interstitials, show a stronger improvement with pressurization, with n ~ 0.3.[14] Infiltrated electrodes are an important electrode class that has been shown to achieve low R_P at low operating temperature. Aside from one previous report,[14] however, results on the high pressure characteristics of infiltrated electrodes are extremely limited. Amongst the various infiltrants studied, Praseodymium oxide (PrO_x) has been shown to provide some of the lowest R_P values.[19-22] PrO_x features high electronic and ionic conductivities along with excellent activity for the oxygen reduction reaction in the temperature range of interest, likely stemming from a high concentration of oxygen ion vacancies.[19]

Here we report on the low temperature (550-650 ˚C) impedance characteristics versus p_{O_2}, from 0.1 up to 8 atm, for two recently developed oxygen electrodes of interest for LT-SOCs: $SrTi_{0.3}Fe_{0.63}Co_{0.07}O_{3-\partial}$ (STFC) and PrO_x-infiltrated STFC (STFC:PrO_x). STFC is a perovskite MIEC that has recently been shown to provide relatively low R_P and good stability,[23] and considerable reduction in R_P when infiltrated with PrO_x.[22] The present study is done using electrochemical impedance spectroscopy (EIS) using electrolyte supported symmetric cells in order to directly probe the oxygen electrode, i.e., to avoid interference from a fuel electrode response that would be present in a full cell. The electrolyte is $Ce_{0.9}Gd_{0.1}O_{2-\partial}$ (GDC) in order to avoid any responses associated with the interface between a GDC barrier layer and a YSZ electrolyte. Different impedance contributions are analyzed by fitting the impedance data to a transmission-line-based equivalent circuit modified model informed by a distribution of relaxation times (DRT) analysis. The effect of p_{O_2} and temperature on the electrochemical mechanisms with and without PrO_x is discussed. The combination of infiltration and pressurized operation is shown to achieve desired low-temperature oxygen electrode performance.

2. Results

Figure 1 shows Nyquist and Bode plots of the impedance responses for un-infiltrated (STFC electrode) and infiltrated (STFC:PrO_x electrode) symmetric cells, measured at 650 ˚C over a range of oxygen partial pressures (p_{O_2}). Similar plots for data measured at 550 and 600 ˚C are provided as Figures S1 and S2, respectively, in the supplement. The magnitude of the impedance responses decreases with increasing p_{O_2} for both electrodes. PrO_x infiltration clearly decreases the polarization resistance at all p_{O_2} values, with the low frequency (~1 Hz) response that is important at low p_{O_2} for STFC especially decreased in STFC:PrO_x.

Figure 2 illustrates the EIS responses of the STFC and STFC:PrO_x cells measured at p_{O_2} = 4 atm and various temperatures. The results show the expected decrease in total polarization resistance R_P with increasing temperature. The figure also highlights the substantial reduction in R_P resulting from PrO_x infiltration.

Figure 3 shows a plot of the total polarization resistance R_P versus p_{O_2} for both electrodes and each temperature. The STFC:PrO_x electrode cells consistently show much lower R_P values compared to the STFC cells, as also seen in Figures 1 and 2. The R_P versus p_{O_2} data are fitted very well (R^2 > 0.95) by straight lines given by $R_P \propto p_{O_2}^{-n}$, as shown in Figure 3. The n values shown on the plot vary slightly with temperature and are slightly higher for STFC:PrO_x (~0.288-0.333) than for the STFC electrode (~0.234-0.277). Thus, the performance improvements due to PrO_x infiltration are greater at higher pressures. For example, pressurization from p_{O_2} = 0.2 atm (1 atm air) to p_{O_2} = 4 atm (20 atm air) at 600 ˚C decreases R_P for STFC by a factor of 2.1 (from 0.36 to 0.17 Ω cm^{-2}) whereas the same pressurization at 600 ˚C decreases R_P for STFC:PrO_x by a factor of 2.6 (from 0.13 to 0.05 Ω cm^{-2}). Alternatively, PrO_x infiltration decreases R_P by a factor of 2.8 at 600 ˚C for p_{O_2} = 0.2 atm, but decreases R_P by a factor of 3.4 for p_{O_2} = 4 atm.

3. Impedance Modeling

The EIS data is analyzed using an equivalent circuit model (ECM) developed by resolving individual electrode processes with the help of a Distribution of Relaxation Time (DRT) analysis. Figure 4a shows an example of the DRT plots obtained for STFC and STFC:PrO_x cells at p_{O_2} = 1 atm and 600 ˚C. Three distinct peaks along with a possible shoulder peak are resolved. The DRT results are similar to those reported previously for similar STFC and STFC:PrO_x electrode cells at ambient pressure (p_{O_2} = 0.2 atm),[22] and so the same ECM (Figure 4b), along with the same attributions of the three peaks to different electrode processes, are used here. The model includes an R_{int}-Q_{int} element that appears as the high frequency peak and represents oxygen ion transport across the interface between the mixed ionic and electronic conducting (MIEC) electrode and the electrolyte. In series with this is a transmission-line model (TLM) element that represents the porous electrode, including the ionic transport resistance R_i and MIEC/gas surface processes. Note that resistors associated with the electrode's electronic transport are not included in the TLM, as usual for MIEC oxygen electrodes, because they are negligibly small compared with R_i.[22, 25] The latter includes an element R_{rxn}-Q_{rxn} that appears as the medium frequency response and represents the oxygen surface exchange reaction, nested with an element R_{surf}-Q_{surf} that represents a surface process (low frequency response). This combined circuit element was introduced by Meyer et al.[24] to simulate a porous electrode with a surface layer; in the present case this may represent the Sr-rich layer on the MIEC surface.[22] The modified TLM is used instead of a Gerischer element, often used to model porous MIEC electrodes, because it provides a good fit to both the low- and midfrequency responses and because the present electrodes are relatively thin (see Figure S3), such that the thick-electrode limit epitomized by the Gerischer element may not be satisfied.[22] Note that the high frequency shoulder on the P_{rxn} response (Figure 4a) arises directly from the TLM and so there is no need for a separate circuit element to model this.[22] The GDC electrolyte resistance is modeled using a resistor R_{el} and is given approximately by the first x-intercept of the real impedance response on the Nyquist plot. Finally, an inductor element L_{ind} is included to account for measurement-circuit inductances that affect the high frequency response.

Figure 5 illustrates representative ECM fits highlighting the contributions of the different electrode processes in Nyquist plots of EIS data taken at 550 ºC with p_{O_2} = 0.2 atm and 4 atm from STFC and STFC:PrO_x cells. For the STFC electrode, the reaction contribution represents the dominant impedance response; the surface layer contribution is smaller, especially at the higher p_{O_2}, and the electrode/electrolyte interface response is relatively small. For STFC:PrO_x, the electrode reaction response is much reduced compared to the STFC case, and the surface response is essentially eliminated. That is, PrO_x infiltration increases the rates of the oxygen transport processes at the MIEC/gas interface. On the other hand, the high frequency electrode/electrolyte interface response is little changed, or even slightly increased, by PrO_x infiltration, and pressurization also has little effect. This is not surprising for a solid/solid interface process. As a result of these changes, the reaction process that is dominant for p_{O_2}= 0.2 atm decreases enough that the interface process is comparable in magnitude at p_{O_2} = 4 atm. Indeed, where the reaction response is at its lowest, for STFC:PrO_x under pressure, the interface response is dominant.

4. Discussion

The R_{rxn}, R_{int}, and R_{surf} values obtained from fits such as those shown in Figure 5 are plotted versus p_{O_2} in Figure 6. The results are used here as the basis to discuss the associated mechanisms. The oxygen reaction resistance R_{rxn} variation with p_{O_2} (Figure 6a) is fitted reasonably well using a power law with n ~ −0.19-0.26 for STFC compared to n ~ −0.49-59 for STFC:PrO_x. In general, a power law of ~ 0.25 is often explained as a charge transfer process,[26-29] whereas a power law of ~ 0.5 is usually attributed to a dissociative adsorption process.[30, 31] A possible conclusion is that PrO_x nanoparticles on STFC provide an alternative fast pathway for the oxygen surface exchange reaction that is limited by adsorption rather than charge transfer. Arrhenius plots of R_{rxn} versus inverse temperature (See Figure S3) were generally quite linear, but the resulting activation energies are approximate because only three temperatures were measured. The estimated activation energy for R_{rxn}, ~ 1.2 eV, is reduced by ~ 0.1 eV for STFC:PrO_x (the values are essentially independent of pressure). This change, though small, is consistent with the idea that PrO_x provides an alternate reaction pathway scaffold. PrO_x has been shown via density functional theory[19] and experiment[22] to provide a different path for oxygen adsorption and desorption as a result of lower surface energies associated with oxygen transfer compared to perovskite oxides like STFC or LSCF.

The resistance R_{int} varies little with p_{O_2} in Figure 6b, supporting its assignment as the resistance for oxygen transport across the electrode/electrolyte (solid/solid) interface. The reasons for the slightly higher R_{int} for STFC:PrO_x are not clear. It is possible that significant oxygen transport across the STFC:PrO_x/GDC interface occurs via PrO_x, and it may have a higher resistance than that of STFC alone. Note that the power law values of R_P shown in Figure 3 are consistent with the results in Figure 6: for STFC:PrO_x, both R_{int} and R_{rxn} contribute significantly to R_P, such that its p_{O_2} dependence is intermediate between that of it two components, whereas for STFC,

R_P's p_{O_2} dependence is close to that of its dominant R_{rxn} component.

The resistance R_{surf} (Figure 6c) is small compared to the other resistances for STFC. Indeed, it is so small as to be un-measurable for p_{O_2} > 1 atm for STFC:PrO_x. As discussed by Lu et al.,[22] this additional element in the TLM is added to account for the presence of a surface layer on a porous electrode, in this case presumably the segregated SrO layer.[22, 24] The power law exponent is relatively large, from -0.5-0.8; the physical interpretation of this exponent is unclear at this point. The substantial reduction of R_{surf} by PrO_x infiltration agrees with a prior report;[22] it is suggested that PrO_x may reduce the SrO surface layer thickness or provide an alternative pathway for oxygen transport.

R_i values obtained from the fits (see Figure S5) show no discernable trend with p_{O_2} with considerable scatter in the range from ~1000 to 5500 Ω cm; these values are similar to those reported by Lu et al. for STFC and STFC:PrO_x.[22] One possible explanation is that these electrodes are in the thin-electrode limit, *i.e.*, the active depth λ of the electrode is larger than its thickness L, such that the polarization is not significantly limited by ionic transport. This idea is checked by estimating the active depth,

$$\lambda = \sqrt{\frac{R_{rxn} + R_{surf}}{R_i}} \qquad \textbf{(Eq. 1)}$$

using values from the EIS fits. This yields values greater than 14 μm (see Figure S6), larger than L ~ 8 - 12 μm for the present electrodes, verifying that they are in the thin-electrode limit. The shape of the EIS arcs, *e.g.,* in Figure 5, i.e., are symmetric rather than Gerischer shaped, also consistent with the thin-electrode limit.

The present results can be compared with a prior pressurization study[14] that included infiltrated electrodes. Those data are compared with the present data at a common temperature, 550 ˚C, in Figure S7. Besides having a factor of ~ 10 times lower R_P values than the previous infiltrated electrodes, the present results show higher n values, ~ 0.25 for STFC and ~ 0.3 for STFC:PrO_x compared to n = 0.24 for a $Pr_2NiO_{4+\delta}$ infiltrated $La_{0.80}Sr_{0.20}Ga_{0.80}Mg_{0.20}O_{3-\delta}$ (LSGM) electrode and n = 0.15 for a $(Sm_{0.5}Sr_{0.5})CoO_{3-\delta}$ infiltrated GDC electrode.[14]

Regarding the application to pressurized low-temperature SOCs, the present oxygen electrode materials show far better performance under pressurized conditions than the $(La_{0.6}Sr_{0.4})(Co_{0.2}Fe_{0.8})O_3$ (LSCF) electrodes that are now widely used in SOCs. Table 1 shows a comparison of the present polarization resistance values with those previously observed for LSCF versus pressure.[14] The R_P values for STFC and especially STFC:PrO_x at atmospheric pressure are lower than for LSCF, even though the measurement temperature was lower (650 ˚C versus 700 ˚C). Note that the improvement with pressurization observed for LSCF is rather small, as its power-law exponent is only n ~ 0.11. Thus, the values at p_{O_2} = 4 atm are much lower (2x better for STFC and 6x better for STFC:PrO_x) compared to LSCF; again, this is despite the lower temperature.

5. Conclusions

The reduction in polarization resistance by increasing p_{O_2} from 0.1 – 8 atm follows a power law dependence with a larger exponent (~0.3) for STFC:PrO_x |GDC symmetric cells compared to STFC |GDC symmetric cells (~0.25). That is, the PrO_x-infiltrated electrodes, which yield substantially better performance in air, realize even higher performance gains with pressurization. Analysis of electrochemical impedance spectroscopy data shows that PrO_x infiltration substantially reduces both the surface reaction resistance and the resistance attributed to Sr surface segregation. Different power law slopes suggest a switch to an adsorption-limited process for STFC:PrO_x compared to a charge-transfer-limited process for STFC. Pressurization of the STFC:PrO_x electrode to ≥ 4 atm results in extremely low polarization resistance values – the surface process resistances are so small in this case that the electrode/electrolyte interface resistance becomes the dominant loss. Thus, further improvements in such electrodes may require a focus on reducing this interfacial resistance.

6. Experimental Procedures

Cell Fabrication

Symmetric cell electrolytes were prepared using 0.5 g of gadolinium doped ceria powder pressed at 2 metric tons into pellets that were then sintered at 1450 ˚C for 6 h. Then, two layers of STFC ink were screen printed on opposite sides of the electrolyte with 0.5 cm^2 areas, followed by sintering at 1050 ˚C for 2 h. For the PrO_x solution, a 1 M solution was prepared in a similar fashion as described previously.[22] Briefly, $Pr(NO_3)_3.6H_2O$ (Sigma-Aldrich) was dissolved in deionized water with added surfactant Triton X-100 to achieve a final concentration of 1 M. The mixture was stirred for 24 hours before 2 μL was added to the active area in a single step infiltration. Excess solution was removed using a cotton swab. Silver paste (Heraeus) was screen printed as a grid onto to each side for current collection.

Pressurized testing and electrochemical impedance spectroscopy (EIS)

A custom pressurized furnace system (Deltech Furnaces Inc, Denver, CO) described in more detail elsewhere[11, 14] was used for measurements at temperatures of 550, 600 and 650˚C and oxygen partial pressures p_{O_2} of 0.1 to 8 atm. This would correspond to air at pressures from 0.5 atm to 40 atm. p_{O_2} values from 1 to 8 atm were obtained by pressurizing pure O_2 (g), whereas values between 0.1 and 1 atm were obtained with O_2-N_2 mixtures at a total pressure of 1 atm. Total flow rate was kept at 200 standard cubic centimeters per minute (sccm) for every pressure tested. Electrochemical impedance spectroscopy data was obtained using a SquidStat Plus (Admiral Instruments) unit in a frequency range from 0.1 – 10^6 Hz and an excitation amplitude of 20 mV in a 4-point setup.

Distribution of relaxation times analysis was performed using a MATLAB script developed by Wan et al.[32]. Also, for DRT, a regularization parameter factor of 10^{-3} was chosen. The equivalent circuit model shown in Figure 4 has been used for similar symmetric cells in previous work.[22] Equivalent circuit modeling was done using custom Python scripts and a complex nonlinear least square solver.

Total polarization resistance values are calculated from the ECM fit. This is done to provide a more accurate value than simply taking the real-axis intercepts which would require extrapolation since the very low frequency impedances often do not reach the real axis. This is evident, for example, in Figure 1a where the low frequency responses for the lowest oxygen partial pressures remain above the x-axis.

Microstructural Imaging

For analysis purposes, the electrode thickness was verified using a JEOL 9700 SEM and thicknesses of 12 μm and 8 μm were used while modeling for the pristine (a) and infiltrated cells (b) respectively. Figure S4 shows the SEM micrographs.

7. Acknowledgements

The authors gratefully acknowledge financial support by the U.S. Department of Energy, Office of Energy Efficiency and Renewable Energy, Fuel Cell Technologies Office, under Award

Number DE- EE0008437, and the National Science Foundation (OISE-1545907). This work made use of the EPIC facility of Northwestern University's NUANCE Center, which has received support from the SHyNE Resource (NSF ECCS-2025633), the IIN, and Northwestern's MRSEC program (NSF DMR-1720139)

Competing interests

The authors declare no competing interests.

8. Figures

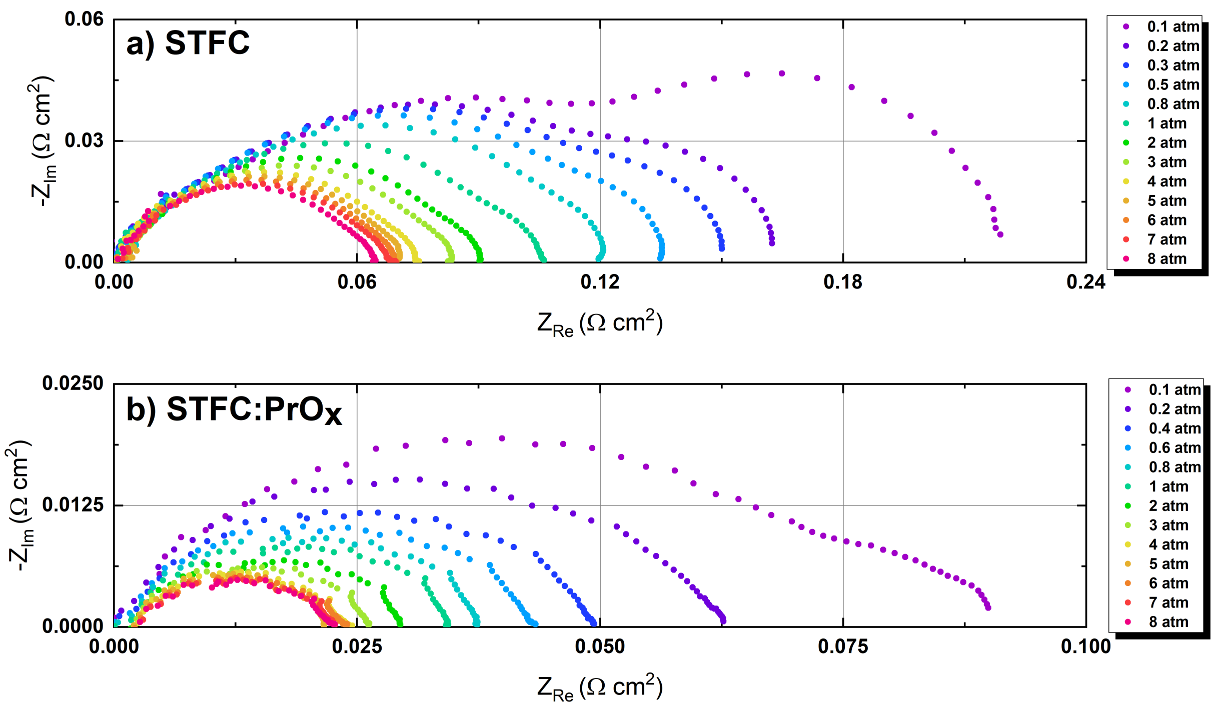

Figure 1. *Nyquist plots for for a) GDC|STFC and b) GDC|STFC:PrO$_x$ cells at 650˚C for oxygen partial pressures from 0.1 atm to 8 atm.*

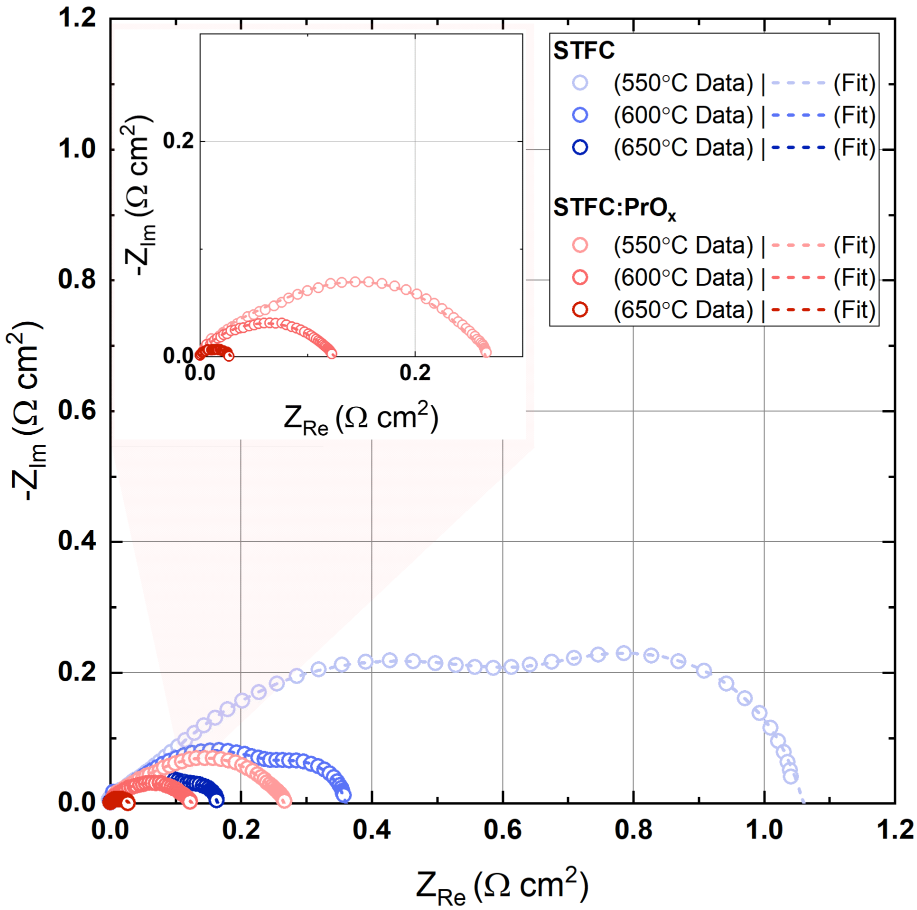

Figure 2. *Nyquist plots for STFC and STFC:PrO$_x$ electrode cells showing the response for different temperatures at an oxygen partial pressure of 4 atm. The inset at the top left provides a magnified view of the responses near the origin. The fitted curves shown are from the equivalent circuit model (ECM) discussed in section 3.*

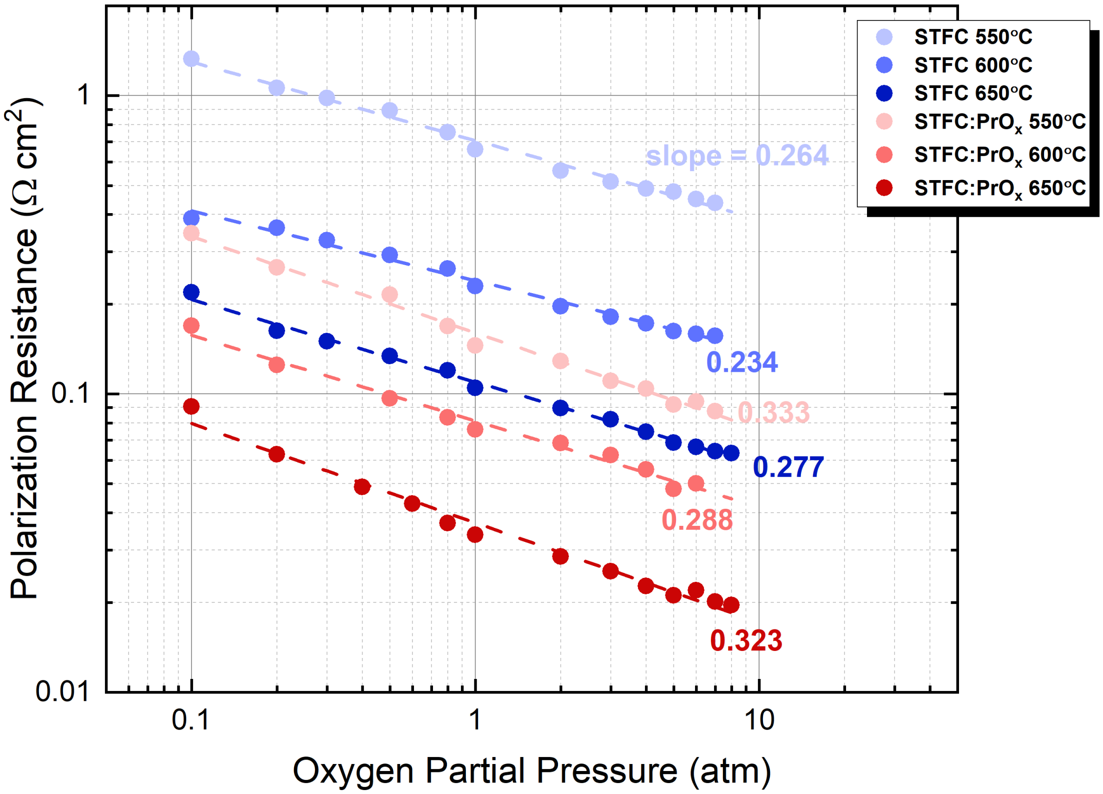

Figure 3. *Log-Log plot of total polarization resistances R_P versus oxygen partial pressure at various temperatures for GDC|STFC and GDC|STFC:PrO_x cells. The R_P values are obtained from equivalent circuit model fits of the EIS data, as discussed in section 3. A power law equation of the form $R_P \propto p_{O_2}^{-n}$ is fit to the data and the exponent n is shown for each case.*

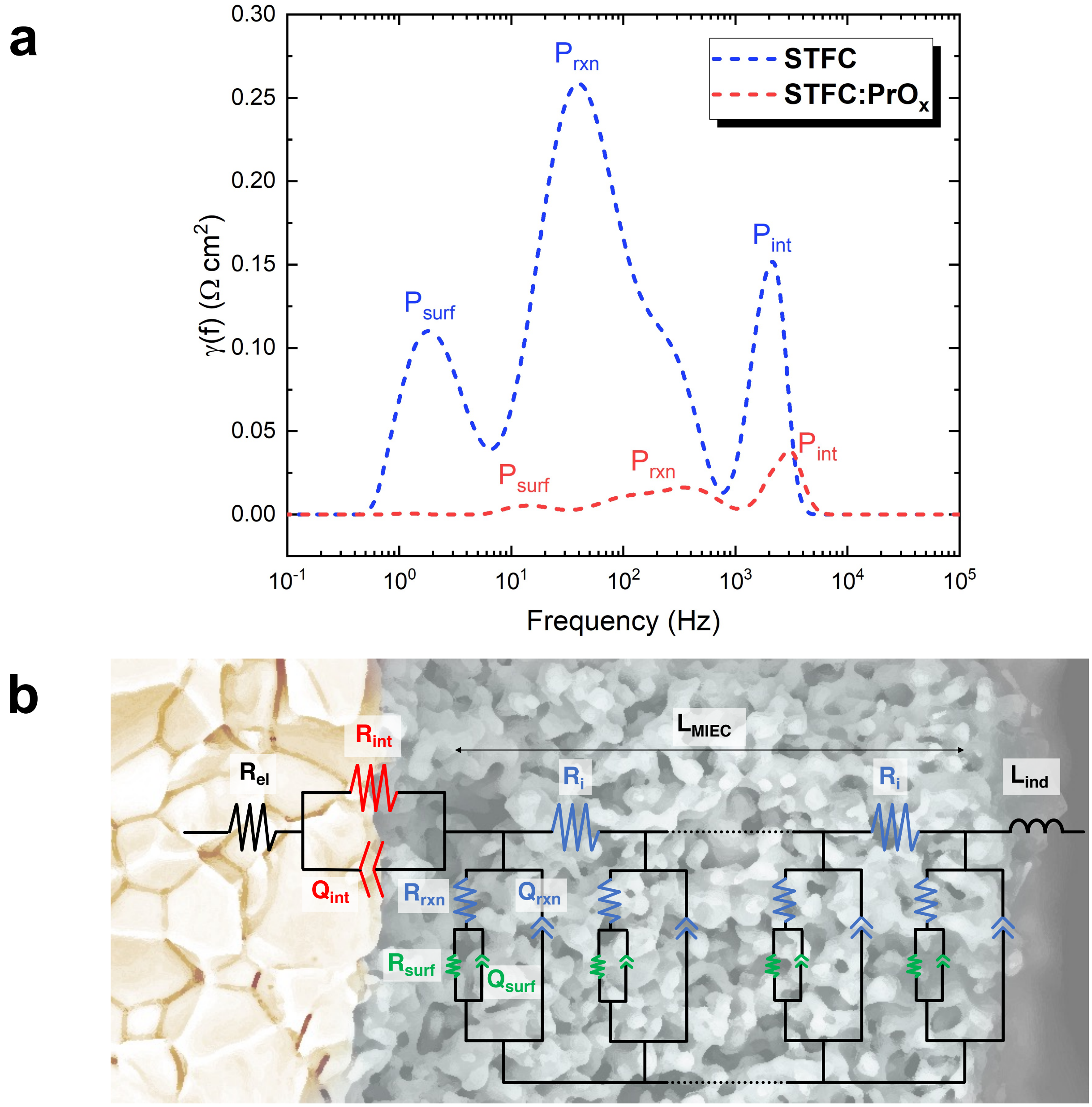

Figure 4. *A) DRT analysis result for GDC|STFC and GDC|STFC:PrO$_x$ cells at p_{O_2} = 1 atm and 600 ˚C. The low frequency peaks are attributed to a surface layer on the electrode, the medium frequency peaks to the reaction at the electrode/gas interface, and the high frequency peaks to ion transport across the electrode/electrolyte interface. B) The equivalent circuit model used for fitting the EIS data.*

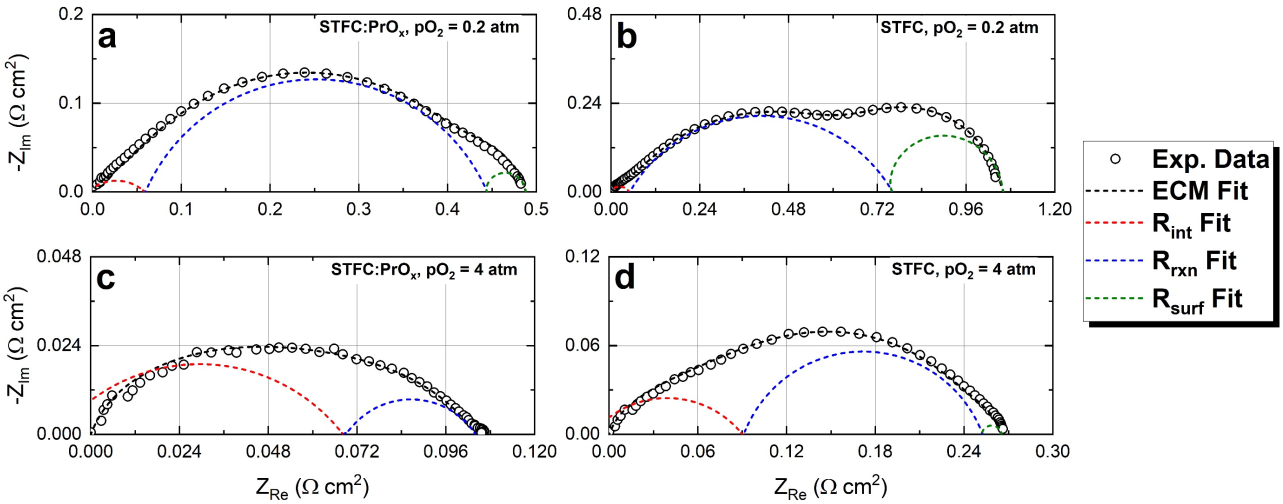

Figure 5. *Nyquist (a-d) plots of equivalent circuit model fits to EIS data taken at 550 ˚C for oxygen partial pressures of 0.2 atm (the partial pressure of O_2 in air) and 4 atm (corresponding to an air pressure of 20 atm), for STFC and STFC:PrO_x electrode cells. The individual components of the fits, including the interface, reaction and surface contributions, are shown as dashed lines. The surface layer response is found to be negligible within the margin of error in ECM fitting for p_{O_2} ≥ 1 atm at all temperatures, such that the (R_{Surf}, Q_{Surf}) component is set to zero for these fits. Deconvolution of the TLM contributions is done as follows: the TLM response with just the reaction element R_{rxn}-Q_{rxn}, i.e., with no R_{surf}-Q_{surf} element, was plotted using the R_{rxn} and Q_{rxn} values from the overall ECM fit, and the R_{surf}-Q_{surf} element response shown is just the difference between this and that of the overall modified TLM.*

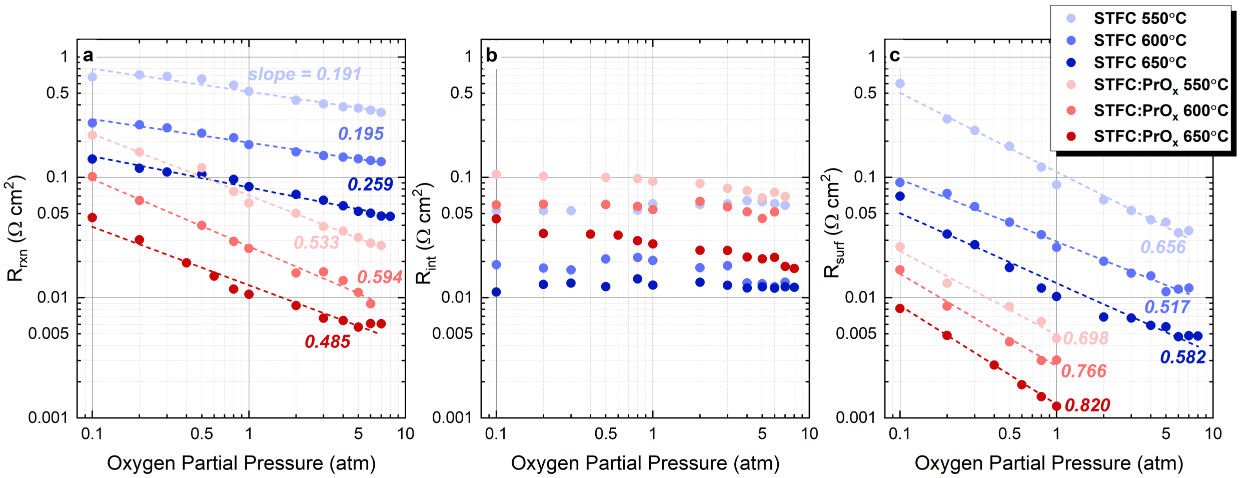

Figure 6. *Log-Log plots of reaction resistance (a), interface resistance (b), and adsorption resistance (c) versus oxygen pressure for STFC and STFC:PrO$_x$ at different temperatures, derived from ECM fits to the EIS data. Fits to the data of the form $R \propto p_{O_2}^{-n}$ are shown and the n values are given.*

Table 1. Polarization resistance values for various electrodes versus pressure

Pressure	Polarization Resistance R_P (Ω-cm^2)		
	STFC (650 ˚C)	STFC:PrO$_x$ (650 ˚C)	LSCF (700 ˚C)[14]
p_{O_2} = 0.2 atm (1 atm air)	0.163	0.063	0.19
p_{O_2} = 4 atm (20 atm air)	0.075	0.023	0.14

LSCF data from Railsback et al.[14]

9. References

1. R. J. Braun and P. Kazempoor, in *Energy and Environment Series*, M. Ni and T. S. Zhao, eds., p. 327-382, Royal Society of Chemistry, Cambridge, (2013).
2. F. Calise and M. Dentice d'Accadia, in *Solid Oxide Fuel Cells*, p. 383-462, (2013).
3. S. H. Jensen, X. Sun, S. D. Ebbesen, R. Knibbe, and M. Mogensen, *International Journal of Hydrogen Energy,* **35** (18), 9544-9549 (2010).
4. S. H. Jensen, C. Graves, M. Mogensen, C. Wendel, R. Braun, G. Hughes, Z. Gao, and S. A. Barnett, *Energy & Environmental Science,* **8** (8), 2471-2479 (2015).
5. C. H. Wendel, Z. Gao, S. A. Barnett, and R. J. Braun, *Journal of Power Sources,* **283** 329-342 (2015).
6. Q. Cacciuttolo, J. Vulliet, V. Lair, M. Cassir, and A. Ringuedé, *International Journal of Hydrogen Energy,* **40** (35), 11378-11384 (2015).
7. E. P. Reznicek and R. J. Braun, *Applied Energy,* **259** (2020).
8. X. Sun, M. Chen, S. H. Jensen, S. D. Ebbesen, C. Graves, and M. Mogensen, *International Journal of Hydrogen Energy,* **37** (22), 17101-17110 (2012).
9. C. H. Wendel and R. J. Braun, *Applied Energy,* **172** 118-131 (2016).
10. C. H. Wendel, P. Kazempoor, and R. J. Braun, *Journal of Power Sources,* **301** 93-104 (2016).
11. G. Hughes, J. Railsback, D. Butts, and S. A. Barnett, *ECS Transactions,* **68** (1), 687-697 (2015).
12. S. H. Jensen, H. Langnickel, N. Hintzen, M. Chen, X. Sun, A. Hauch, G. Butera, and L. R. Clausen, *Journal of Energy Storage,* **22** 106-115 (2019).
13. S. H. Jensen, X. Sun, S. D. Ebbesen, and M. Chen, *Fuel Cells,* **16** (2), 205-218 (2016).
14. J. Railsback, G. Hughes, L. Mogni, A. Montenegro-Hernández, and S. Barnett, *Journal of The Electrochemical Society,* **163** (13), F1433-F1439 (2016).
15. Z. Gao, L. V. Mogni, E. C. Miller, J. G. Railsback, and S. A. Barnett, *Energy & Environmental Science,* **9** (5), 1602-1644 (2016).
16. Z. Shao and S. M. Haile, **431** 4 (2004).
17. Y. Xia, Z. Jin, H. Wang, Z. Gong, H. Lv, R. Peng, W. Liu, and L. Bi, *Journal of Materials Chemistry A,* **7** (27), 16136-16148 (2019).
18. E. C. Thomsen, G. W. Coffey, L. R. Pederson, and O. A. Marina, *Journal of Power Sources,* **191** (2), 217-224 (2009).
19. Y. Chen, Y. Chen, D. Ding, Y. Ding, Y. Choi, L. Zhang, S. Yoo, D. Chen, B. deGlee, H. Xu, Q. Lu, B. Zhao, G. Vardar, J. Wang, H. Bluhm, E. J. Crumlin, C. Yang, J. Liu, B. Yildiz, and M. Liu, *Energy & Environmental Science,* **10** (4), 964-971 (2017).
20. D. Ding, X. Li, S. Y. Lai, K. Gerdes, and M. Liu, *Energy & Environmental Science,* **7** (2), (2014).
21. P. V. Hendriksen, M. Khoshkalam, X. Tong, Đ. Tripković, M. A. Faghihi-Sani, and M. Chen, *ECS Transactions,* **91** (1), 1413-1424 (2019).
22. M. Y. Lu, R. Scipioni, B.-K. Park, T. Yang, Y. A. Chart, and S. A. Barnett, *Materials Today Energy,* **14** (2019).
23. S.-L. Zhang, H. Wang, M. Y. Lu, A.-P. Zhang, L. V. Mogni, Q. Liu, C.-X. Li, C.-J. Li, and S. A. Barnett, *Energy & Environmental Science,* **11** (7), 1870-1879 (2018).
24. J. P. Meyers, M. Doyle, R. M. Darling, and J. Newman, *Journal of The Electrochemical Society,* 12 (2000).
25. S.-L. Zhang, D. Cox, H. Yang, B.-K. Park, C.-X. Li, C.-J. Li, and S. A. Barnett, *Journal of*

Materials Chemistry A, **7** (37), 21447-21458 (2019).
26. S. Adler, X. Chen, and J. Wilson, *Journal of Catalysis,* **245** (1), 91-109 (2007).
27. S. Linquette-Mailley, *Solid State Ionics,* **107** (3-4), 191-201 (1998).
28. Y. Takeda, R. Kanno, M. Noda, Y. Tomida, and O. Yamamoto, *Journal of The Electrochemical Society,* **134** (11), 2656-2661 (1987).
29. D. Y. Wang and A. S. Nowick, *Journal of The Electrochemical Society,* **126** (7), 1155-1165 (1979).
30. J. Ascolani-Yael, A. Montenegro-Hernández, Q. Liu, S. A. Barnett, and L. Mogni, *Journal of The Electrochemical Society,* **166** (16), F1301-F1307 (2019).
31. E. Siebert, A. Hammouche, and M. Kleitz, *Electrochimica Acta,* **40** (11), 1741-1753 (1995).
32. T. H. Wan, M. Saccoccio, C. Chen, and F. Ciucci, *Electrochimica Acta,* **184** 483-499 (2015).